Journal of Structural Geology 186 (2024) 105218

Contents lists available at ScienceDirect

Journal of Structural Geology

journal homepage: www.elsevier.com/locate/jsg

Damage asymmetry of the Chimei Fault, eastern Taiwan, and implications for deformation evolution

Szu-Ting Kuo [a,*], Larry Syu-Heng Lai [b], En-Chao Yeh [c], Yi-Ling Tsai [a], Li-Wei Kuo [a,d]

[a] Department of Earth Sciences, National Central University, 320317, Taoyuan, Taiwan
[b] Department of Earth and Space Sciences, University of Washington, Seattle, WA, 98195, United States
[c] Department of Earth Sciences, National Taiwan Normal University, 116059, Taipei City, Taiwan
[d] Earthquake-Disaster & Risk Evaluation and Management (E-DREaM) Center, National Central University, 320317, Taoyuan, Taiwan

ARTICLE INFO

Keywords:
Chimei Fault
Fault damage zone
Paleostress analysis
Deformation modes
Collisional basin

ABSTRACT

The mesoscale deformation structures in eastern Taiwan are considered to have recorded progressive deformation during rapid convergence and uplift in response to arc-continent collision. However, detailed deformation mechanisms and kinematic history of faulting remained poorly known. The Chimei Fault in eastern Taiwan thrusts the igneous forearc basement over the orogen-derived turbidites, and its outcrops provide opportunities to understand deformation mechanisms of the fault rocks across a bi-material fault during the arc-continent collision. To unravel the structural and mechanical architecture of the Chimei Fault, we performed field observations, paleostress analysis, and fold analysis. The Chimei Fault shows a fault core surrounded by damage zones. The width of the damage zones across the fault core is asymmetric, with the footwall turbidites exhibiting wider damage zone with higher fracture intensity than the hanging wall andesitic complex. Our paleostress analysis reveals that the mechanically stronger hanging wall can accommodate larger differential stress than the weaker footwall. Different deformation styles in the footwall damage zones, including pinch-and-swell structures, boudins, and postdating fractures, suggesting progressive deformation while sediment lithification in response to the activities of the Chimei Fault.

1. Introduction

Fault zones play a key role in the deformation of the upper crust in the Earth, controlling the mechanics and hydrological properties of the crust and the architecture of sedimentary deposits in basins (e.g., Caine et al., 1996; Faulkner et al., 2010). Field- and drilling-based observations have provided different structural features of fault zones in different types of faulting regimes (Chester et al., 1993; Chester and Chester, 1998; Berg and Skar, 2005; Rawling and Goodwin, 2006; Ma et al., 2006; Mitchell et al., 2011; Li et al., 2013). For example, mature strike-slip fault systems developed in crystalline and lithified rock units have developed structural features with several components that have been widely recognized: (1) a less deformed *protolith* as the host rock, (2) *damage zones* containing fractures and fissures adjacent to the principal slip zone in the hanging wall and the footwall, and (3) a *fault core* that accommodates most of the displacement during fault movement and consists of cataclasite or fault gouge (Sibson, 1977; Chester and Logan, 1986; Chester et al., 1993; Caine et al., 1996). Identification of damage zone width is based on the presence of fractures and the associated fracture density variation that mark the termination of the protolith, with the development of subsidiary brittle faults, veins, joints, stylolites, cleavages and folds (e.g., Mcgrath and Davison, 1995; Caine et al., 1996; Kim et al., 2004; Song et al., 2007; Li et al., 2013; Cao et al., 2024).

In a bi-material fault zone with a fault core that juxtaposes crystalline rocks onto sedimentary rocks with fabrics developed, the fracture density is greater in the crystalline rocks, while the sedimentary rocks with fabrics developed is relatively undeformed (Mitchell et al., 2011; Aben et al., 2017; Smith and Griffith, 2022; Li et al., 2013). On the other hand, fault zone that develops across the same type of lithology has been documented; for example, fracture density data of the Taiwan Chelungpu Fault Drilling Project (TCDP) reveals that even within the same lithology, fracture density can vary significantly across the fault zone, possibly related to the stress path that fault rock has experienced (Song et al., 2007).

Fault-zone architecture in poorly lithified and siliciclastic rocks exhibits a more complex structural feature, where the fault core is flanked

---

* Corresponding author. Department of Earth Sciences, National Central University 320317, Taoyuan City, Taiwan.
E-mail address: teddythebest_tw@proton.me (S.-T. Kuo).

https://doi.org/10.1016/j.jsg.2024.105218
Received 29 November 2023; Received in revised form 5 July 2024; Accepted 24 July 2024
Available online 25 July 2024

by structurally and lithologically mixed zones (e.g., Rawling and Goodwin, 2006; Nicol and Childs, 2018; Palladino et al., 2018; Pizzati et al., 2023). Brittle and ductile processes coexist in the mixed zones, in which macroscopically ductile structures formed by sediment disaggregation and penetrative particulate flow are crosscut by deformation bands, indicating a temporal and mechanical shift in deformation modes. For the growth of faults in clay-rich and fine-grained sediments undergoing consolidation, progressive deformation generates dewatering structures along the slip surfaces, as has been well documented in drilling cores recovered from subduction zones (Moore and Byrne, 1987; Maltman, 1998; Chester et al., 2013; Savage et al., 2021). The structural features related to progressive deformation are controlled by (1) early-stage soft-sediment deformation that expels excess pore-fluid pressure, such as mud-filled veins asymmetric folds, and boudinages and by (2) latter-stage localized brittle deformation after the sediments have become overconsolidated (i.e., when the sediments are unloaded from the maximum stress state that they have experienced), including shear-induced fractures and disaggregation bands. It is worth noting that the transition from ductile to brittle behavior in soft sediments differs from the “brittle-ductile transition” (BDT) at crustal depth (e.g., Kohlstedt et al., 1995). In this research, we refer to deformation mechanisms that specifically focus on the progressive deformation of soft sediments (Lundberg and Moore, 1986; Moore and Byrne, 1987; Maltman, 1998; Fagereng et al., 2019), and define “brittle” as exhibiting the occurrence of discrete faults and fractures, and “ductile” as referring to dismembered layering and stratal disruption such as (but not limited to) asymmetric folds, boudins, mud-filled veins, and pinch-and-swell structures.

Mesoscale structures in the turbidites in eastern Taiwan are considered to have experienced progressive deformation during the early stages of lithification, coeval with the arc-continent collision (Teng et al., 2002). However, detailed deformation mechanisms and kinematic history of faulting in response to rapid convergence and uplift remained poorly known (Lai et al., 2022). We present field observations, paleostress analysis, and fold analysis of the Chimei Fault, which juxtaposes crystalline igneous rocks and progressively deforming sedimentary rocks. The integration of field-based observations and paleostress analysis allows us not only to investigate kinematic history of the Chimei Fault, but also to unravel the evolution of deformation mechanisms in response to the arc-continent collision.

2. Geological background and outcrop location

The Taiwan Orogeny is the consequence of an active arc-continent collision between the Philippine Sea Plate and the Eurasian Plate (Chai, 1972; Teng, 1990) with a relative plate movement rate of 8 mm/yr (Yu et al., 1997) (Fig. 1). To the east of the onshore suture zone (the Longitudinal Valley Fault; Fig. 1), the Coastal Range comprises of a deformed collisional basin, a retro-foredeep, developed above the forearc crust of Luzon Arc on the Philippine Sea Plate (Lundberg and Dorsey, 1988; Lai et al., 2021a; Chen et al., 2023). Horizontal shortening of the forearc basement and basin sequence creates a series of *en échelon* faults (Fig. 1) (Barrier and Angelier, 1986; Hsieh et al., 2020).

The Chimei Fault, a major fault cutting across the Coastal Range in eastern Taiwan (Hsu, 1956; Chen and Wang, 1996), accommodates a dominant portion of the post-1 Ma crustal shortening of the overriding plate (Philippine Sea Plate) during the arc-continent collision (Hsieh et al., 2020). The Chimei Fault, striking NNE-SSW and dipping 80°SE, juxtaposes the Miocene arc basement rocks with the Plio-Pleistocene orogen-derived conglomerates and turbidites, and it bends to (N80°E, 80°S) in the middle portion of the fault trace where the fault zone intersects with the Hsiukuluan river at the Chimei village (Lai, 1995; Cheng, 1996; Chen, 2005) (Fig. 2). The main fault core of the Chimei Fault is well exposed due to erosion by the Hsiukuluan river (Figs. 2 and 3). No observable Holocene offset of the river terraces has been recorded across the Chimei Fault in this area (Shyu et al., 2006). However, geodetic measurements detect active vertical slip along the fault zone at ca. 8–9 mm/yr in the last decade (Chen et al., 2021).

The hanging wall of the Chimei Fault is composed of andesite with an intense network of gypsum veins in the host rock, as well as disaggregation bands in the 50-m wide damage zone adjacent to the main fault core. The general pattern and characteristics of the Chimei Fault zone

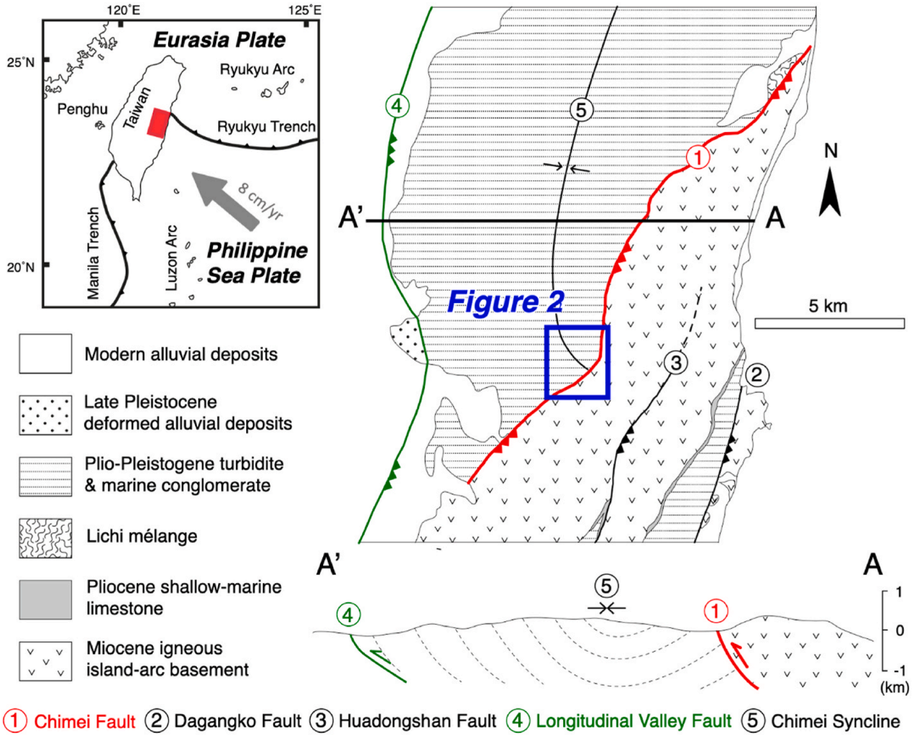

Fig. 1. Tectonic setting and regional geology of the Chimei Fault (modified after Chen and Wang, 1996; Yu et al., 1997; Chang et al., 2001).

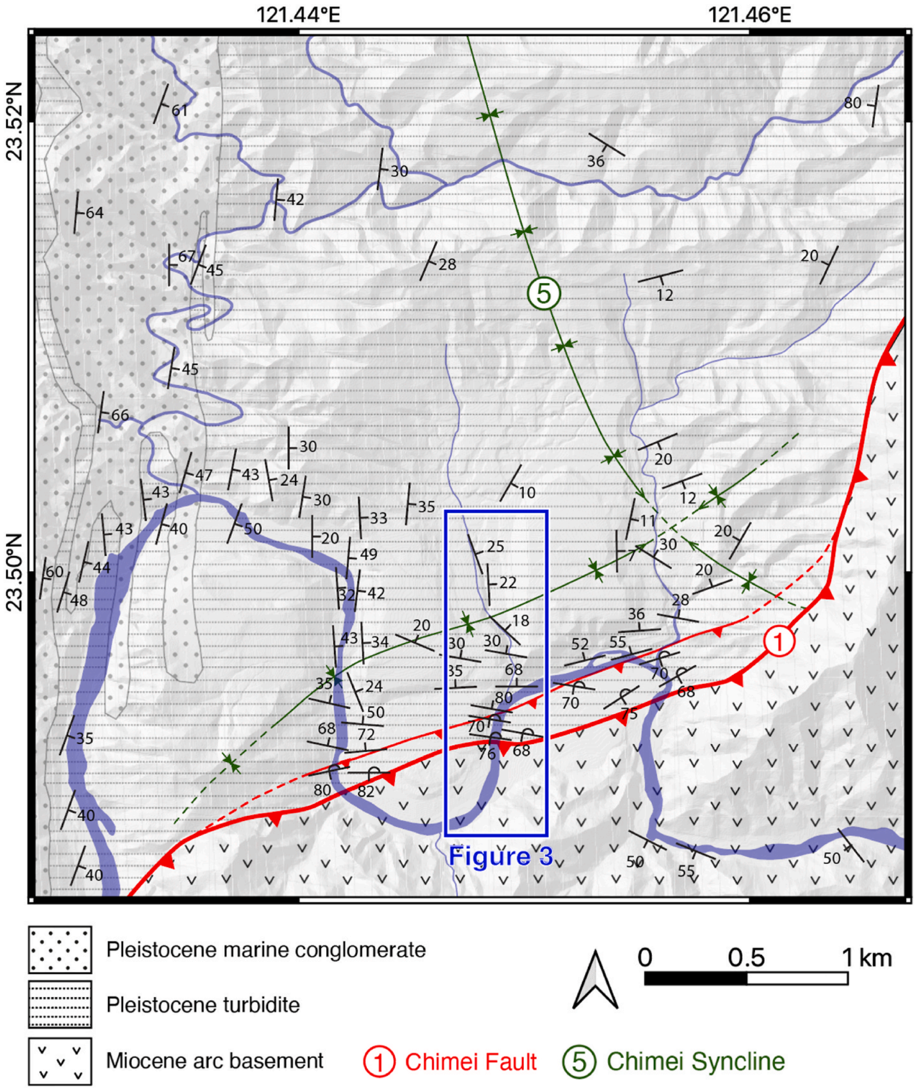

Fig. 2. Regional geological map of the study area near Chimei village (modified after Lai et al., 2022).

have been previously reported (Chen, 2005; Teng et al., 2016). Clay minerals in the altered hanging wall include kaolinite, smectite, and chlorite. Along the lithological boundary, the Chimei Fault develops a fault core with a width of 50 cm. Gouge within the fault core is mainly composed of smectite, chlorite, kaolinite, and illite. The footwall of the Chimei Fault is composed of interbedded siltstone and sandstone, with well-developed folds and small-scale faults in the 800-m wide damage zone. The dominant clay mineral composition includes kaolinite, smectite, chlorite, and illite.

Previous paleostress analysis reveals that the fault movement of the Chimei Fault has both reverse and strike-slip components (Barrier and Angelier, 1986) without a clear crosscutting relationship (Lai, 1995; Cheng, 1996). In this area, compression, as indicated by the averaged axes of the maximum principal stress (σ_1), is nearly perpendicular to the main fault core of the Chimei Fault (Barrier and Angelier, 1986). However, both recent seismicity and geodetic analysis revealed permutation between reverse and strike-slip faulting regime, without significant normal faulting component (Hsu et al., 2009; Chen et al., 2021). In this study, we revisited the Hsiukuluan River section near the Chimei Village (Figs. 1–3) to conduct field observations, paleostress analysis, and fold analysis.

3. Methods

3.1. Fracture density

Fracture patterns and fracture space may reflect contrasts in mechanical properties of different lithologic units (Laubach et al., 2009). To describe the extent of fault damage, we applied the damage zone/fault core model proposed by Chester and Logan (1986). Fault damage zones in the hanging wall and footwall are defined by fracture density of the rock therein, respectively, where both values deviate from background values. Fracture density (N/m) is defined by the number of fractures (N) in a 1-m scanline. We also used fracture space that measures the distance between the two adjacent fractures, together with the fracture space ratio (FSR; corresponding to the mean mechanical layer thickness divided by the median joint spacing) (Gross, 1993), for comparison. We detailed the methodology of obtaining the FSR dataset and the corresponding results in the supplementary material (Table S1-S3 and Fig. S1-S3). We present all datasets in Fig. 3.

3.2. Paleostress and fold analysis

We measured the slickensides on the faults in the hanging wall and footwall damage zones (Figs. 4, 6 and 9) and conducted paleostress analysis based on the multiple inverse method (MIM; Yamaji, 2000).

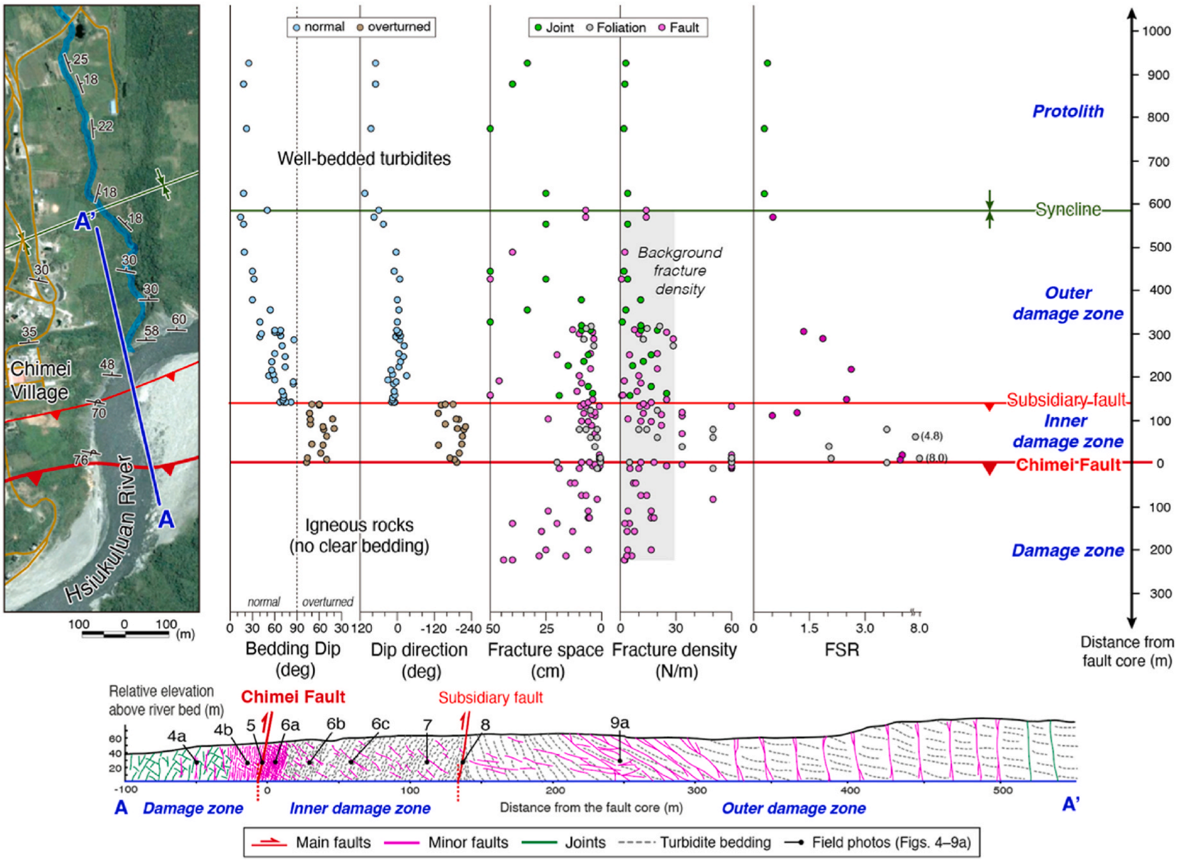

Fig. 3. Fault zone division of the Chimei Fault (Modified after Teng et al., 2016) and the composite outcrop sketch along the Hsiukuluan river. The gray shaded area in the fracture density panel highlights the background range of values (>5 N/m and <30 N/m) in the hanging wall and footwall damage zones.

MIM is built upon the Wallace-Bott hypothesis, which assumes that slip is parallel to the maximum resolved shear stress (Wallace, 1951; Bott, 1959). We followed the workflow suggested by Yamaji (2000) and Sippel et al. (2009): (1) the number of subsets, k, is assigned as 4 in the command prompt window to group the slickenside datasets so that each slickenside is combined with any other 3 slickensides, where $C_k^N/[k!(N-k)!]$ (N is the total number of the data); (2) the MIM software processes all the subsets and calculates the corresponding reduced stress tensor; (3) in the post-processing phase, the MIM software plots the resolved directions of σ_1 and σ_3 in two respective lower hemispheric stereonet, with cold to warm color codes representing stress ratio ranging from 0 to 1 (the black box in Fig. 10). In MIM, the stress ratio, R, is defined as $(\sigma_2-\sigma_3)/(\sigma_1-\sigma_3)$.

To unravel the kinematics of folding, we measured the attitudes of the fold limbs in the footwall inner damage zone and obtained the fold axial planes, fold axes, and fold interlimb angles based on the π-diagram technique (e.g., Cardozo and Allmendinger, 2013). For comparison, we also include the attitudes of the bedding planes in the footwall outer damage zone and the footwall protolith (Fig. 11).

4. Results

4.1. Fracture density and fault zone architecture

The fracture density is generally less than 20 N/m in the crystalline hanging wall, except in the fault rock <3 m from the main fault core, where the fracture density jumps to 60 N/m (the maximum recognizable numbers of fractures we could count at the mesoscale). The fracture space, on the other hand, ranges from <10 cm to 45 cm and does not show significant deviation in the available outcrops. Due to the limited outcrop, the protolith is not recognized. Therefore, we define the exposed hanging wall section of ~220 m width as a fault damage zone.

The fracture density in the footwall which is composed of turbidites increases from 5 N/m to 60 N/m toward the main fault core. One abrupt change in both fracture density and fracture space locates ~620 m from the main fault core, marking the boundary between the protolith and damage zone in the footwall. Another sharp change in fracture density locates ~125 m from the main fault core, which also coincides with the deviations of dip and dip direction in the footwall. With this distinct boundary, we further divided the footwall damage zone into an inner damage zone, adjacent to the fault core, and an outer damage zone, between the inner damage zone and the footwall protolith (Fig. 3). On the other hand, FSR increases from 0.2 in the footwall protolith to 8.0 in the inner damage zone, except that FSR drastically drops around ~125 m from the principal slip zone. It should be noted that fracture space, fracture density, and FSR in the footwall may come out some errors due to the pinch-and-swell structures within the sedimentary beds (Narr and Suppe, 1991; Gross, 1993).

The wall rock in the hanging wall damage zone is yellow to dark red crystalline andesite. No clear layering was observed (Fig. 4a). The fault rock exhibits well-developed anastomosed fractures, and gypsum-filled slickenfiber that crosscut by posterior branch fractures (Fig. 4a) (bulk XRD analysis based on Chen, 2005), and minor faults with fracture density less than 20 N/m (Fig. 3). Approximately 3 m from the main fault core, the hanging wall damage zone becomes a highly sheared dark green body that is dominated by parallel disaggregation bands (Fig. 4b).

A ~0.5 m wide slip zone is distributed along the fault core of the Chimei Fault, with development of 10–15 cm thick of ultracataclasite, intervening gouge layers, cataclasite, and calcite veins (Teng et al., 2016) (Fig. 5). Only a mesoscale description of the fault core is given here, as the fault core and main slip zone are beyond the scope of this study.

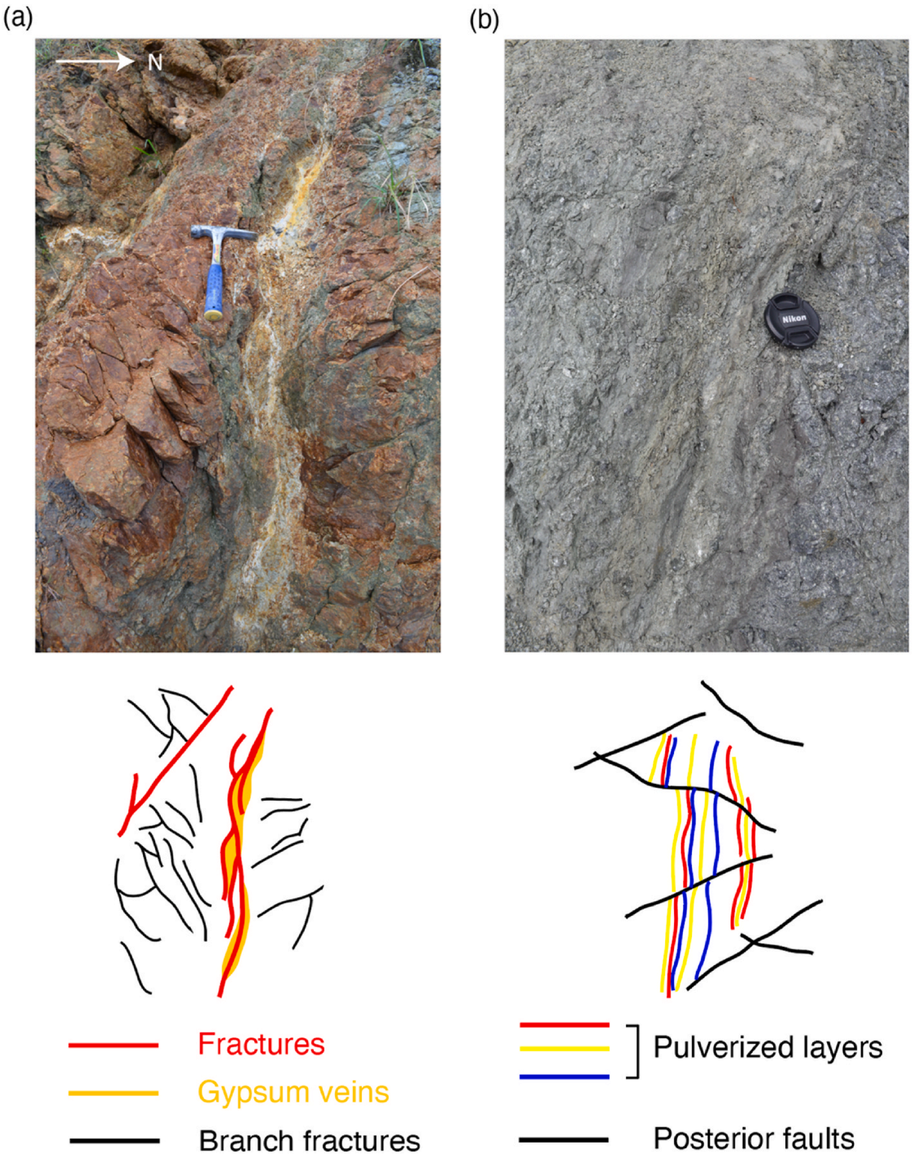

Fig. 4. Mesoscale structures in the hanging wall damage zone: (a) fractures and gypsum veins in the damage zone distanced from the fault core (b) disaggregation bands of andesite adjacent to the fault core.

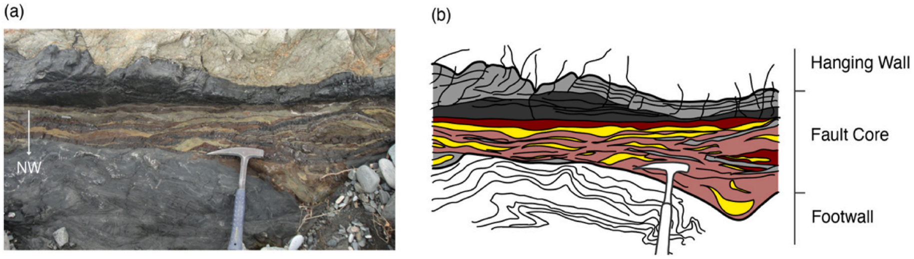

Fig. 5. Mesoscale structure of the fault core.

Adjacent to the fault core of the Chimei Fault on the footwall side, the footwall inner damage zone is composed of overturned interbedded sandstones and mudstones (turbidites) (Figs. 2, 3 and 6). This division exhibits asymmetric Z-folds with rotation within the hinge zone (Fig. 6a), boudins and pinch-and-swell structures (Fig. 6b), fold limbs with different interlimb angles (Fig. 6c), and mud-filled veins (Fig. 7). Bedding-parallel shear can be identified from the thickened sandstone bed (Fig. 6a).

The boundary between the footwall inner and the footwall outer damage zones is marked by a subsidiary fault (Fig. 8). Across the subsidiary fault, dip angle, dip direction, and fracture density change abruptly (Figs. 2 and 3), and this subsidiary fault is a sharp boundary between different failure modes of the fault rocks. The overturned footwall inner damage zone is dominated by ductile deformation behaviors with overprinting brittle deformation, whereas the deformation mode in the footwall outer damage zone normal sequence is only

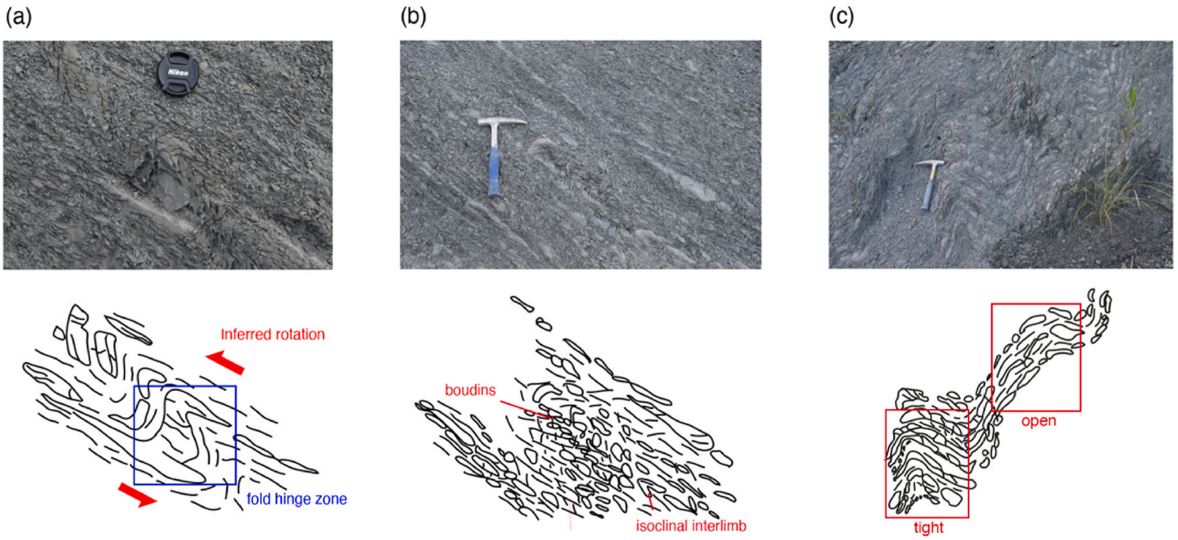

Fig. 6. Fold occurrence in the footwall inner damage zone: (a) inferred rotation of an asymmetric fold. The blue box indicates layer-parallel rotation inferred by the sandstone layer; (b) boudins, pinch-and-swell sandstone, and isoclinal interlimb angle of the fold; (c) open and tight interlimb angles of the folds. The red boxes indicate two examples of different interlimb angles in Fig. 11. (For interpretation of the references to color in this figure legend, the reader is referred to the Web version of this article.)

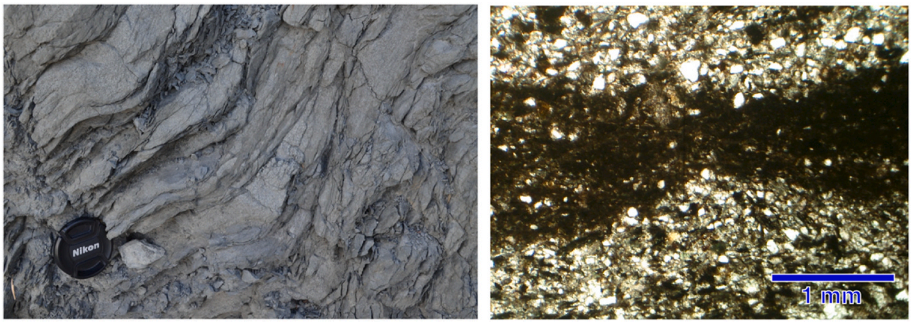

Fig. 7. Mud-filled veins in the footwall inner damage zone at (a) outcrop scale and (b) microscale.

governed by brittle failure. The thicknesses of the sandstone and mudstone beds in the footwall outer damage zone are generally uniform, ranging from several centimeters to ~1 m, and the bedding planes are normal sequence (Figs. 2 and 3). The bedding planes are crosscut by branch faults (Fig. 9a) with fracture density up to 30 N/m (Fig. 3).

The boundary between the footwall outer damage zones and the footwall protolith is marked by a fault-parallel asymmetric syncline, where (1) the bedding trend suddenly changes, (2) the number of the small-scale faults becomes zero, and (3) the background fracture density drops below 5 N/m (Figs. 2 and 3). The footwall protolith is composed of interbedded normal sequence of sandstone and siltstone, with maximum thickness of the sandstone up to 1.5 m (Fig. 9b). The thickness within each bed of sandstone and siltstone is uniform. Albeit without small-scale faults, joints appear in the wall rock of the protolith.

4.2. Paleostress and fold analysis

We present the results of paleostress analysis in Fig. 10. In the hanging wall damage zone, averaged orientations of σ_1- and σ_3-axes are (048°, 11°) and (312°, 27°), respectively, showing an overall strike-slip movement with some reverse component. The σ_1-axes concentrate near the averaged orientation, whereas the σ_3-axes distribute along the great circle perpendicular to the σ_1-axes. The *R* values in this division range from 0.0 to 0.7, with an average of 0.1, indicating that there is a permutation between σ_2 and σ_3.

In the footwall outer damage zone (Fig. 10), averaged orientations of σ_1- and σ_3-axes are (143°, 14°) and (278°, 70°), respectively, showing a general reverse movement. Both σ_1- and σ_3-axes concentrate with respect to their average values in the lower-hemisphere projection. The *R* values in this division range from 0.0 to 1.0, with an average of 0.4.

In the footwall inner damage zone (Fig. 10), averaged orientations of σ_1- and σ_3-axes trend are (321°, 7°) and (216°, 88°), respectively, showing a relatively pure reverse movement comparing to the footwall outer damage zone. The σ_1-axes widely distribute at low angles in the lower-hemisphere projection, whereas the σ_3-axes plunge relatively concentrate near 90°. The *R* values in this division range from 0.5 to 1.0, with an average of 0.9, indicating that there is a permutation between σ_1 and σ_2. Overall, the orientations of σ_1- and σ_3-axes are similar between the footwall outer damage zone and the footwall inner damage zone.

We presented the results of fold analysis in Fig. 12. The pole axes of the bedding planes exhibit a transition from protolith to the footwall inner damage zone, with a rotation of nearly 90° (Figs. 2, 3 and 12). In general, the poles to the fold axial planes in the footwall inner damage zone are concentrated near the north and south poles of the lower-hemisphere projection, suggesting that the compressional orientations of the pure shear orient NW-SE. The compressional orientations are consistent with the orientations of σ_1 obtained from our paleostress analysis (Fig. 10).

Fig. 8. The subsidiary fault marks the boundary between the inner damage zone and the outer damage zone in the footwall.

5. Discussion

5.1. Uncertainties of fracturing density dataset

Compared to the areal and circular scanline techniques, we acknowledge that a linear scanline has its weaknesses and limitations (e. g., Ogata et al., 2017). To this end, we evaluate the uncertainties of the data and address the effects of thickness on the fracture space by obtaining the FSR and comparing the dataset with the original fracture space. In addition, we noted that the normalized fracture space indices, such as fracture space index (FSI) (Bai and Pollard, 2000) and FSR (Gross, 1993), are proposed for joints (i.e., Mode I cracks). The fractures in the footwall inner and outer damage zones of the Chimei Fault, on the other hand, are dominated by shear fractures (Mode II or Mode III cracks). Unlike the extensional/unloading joints which are parallel in strike (Engelder, 1987), shear fractures can develop more complicated structural features and do not necessarily grow perpendicularly to the bedding planes, such as unparallel synthetic and antithetic forms (Kim et al., 2004).

Moreover, bedding thicknesses become more non-uniform toward the principal slip zone in the footwall. Based on our observations, the structural features are dominated by soft-sediment deformation and pinch-and-swell structures are pervasive, such as convoluted and recumbent folds. The geological processes thus are not typical comparing to the outcrops reported for joint spacing measurements.

5.2. Brittle fractures

Across the Chimei Fault, the width of the damage zone in the footwall is larger than that in the hanging wall (Figs. 2 and 3). Such asymmetry in terms of the damage zone width may be a response to the contrast in rock strength (Smith and Griffith, 2022). For a mechanically stronger crystalline igneous rock (e.g., Paterson and Wong, 2005), a larger differential stress is required to create new fractures in an intact protolith or to reactivate the pre-existing faults. In contrast, a progressively deforming footwall sedimentary sequence can accommodate less differential stress until it fails or reactivates. In this study, we propose a simplified scenario that considers stress-strain relationship of the fault rock, the underlying mechanics would follow the fact that the surrounding stress magnitude is capped by the strength of the rock (Kohlstedt et al., 1995). The published uniaxial compressive strength (UCS) data collected in the Coastal Range revealed that the fracture strength of the crystalline igneous rocks (>30 MPa) is higher than that of the turbidites (<20 MPa) (Lai et al., 2021b). It is expected that the igneous rocks can accommodate a larger magnitude of stress and thus require a larger stress to generate permanent deformation over earthquake cycles compared to the turbidites. Thus, during earthquake cycles when stress drop is relatively small and only exceeds the strength of the turbidites, deformation is confined within the footwall, whereas during coseismic events when stress drop is relatively large and exceeds the strength of both andesite and turbidites, deformation can propagate to the hanging wall.

We acknowledge that in contrast to fault cores where structural features can be dominated by shear-induced cataclasites, damage zones that juxtapose crystalline rock and sedimentary rock may encounter sudden extension and become pulverized, such that the crystalline rock usually exhibits a higher degree of deformation than the sedimentary rock with fabrics developed (Mitchell et al., 2011; Aben et al., 2017; Smith and Griffith, 2022). These studies mainly focus on pulverization in response to fracturing under high shot velocity (>5 m/s), and yet fault rocks can host a wide range of slip rates and thus develop various deformation mechanisms over geological time scales in nature (Maltman, 1998; Fagereng et al., 2019; Belzer and French, 2022). According to our field-based observations, the footwall and hanging wall damage zone of the Chimei Fault are dominated by compressional shear-induced fractures, which is consistent with our results of paleostress analysis where orientations of σ_1 in both divisions are nearly horizontal (Fig. 10). Our findings reveal that extension does not play a significant role in either hanging wall or footwall damage zone, which could be a reason why the andesitic hanging wall damage zone is not significantly more deformed than the sedimentary footwall damage zones through pulverization.

Our proposition is thus more inclined to the scenario that rock damage across the fault core is likely controlled by deformation history and stress path (e.g., Song et al., 2007).

Together with the stress ratios (R) based on our paleostress analysis, we schematically illustrate our mechanical interpretation of the damage zones of the Chimei Fault in Fig. 13. We first assume that the brittle deformation within the hanging wall and footwall damage zones resides in revers-faulting regime under the hydrostatic conditions at a similar depth, such that the minimum effective principal stress (σ_3') is equal to the effective overburden stress (σ_V'). We further assume that the intermediate effective principal stress (σ_2') stays constant throughout the brittle deformation. In the footwall, an increase in fracture density leads to a decrease in shear strength toward the principal slip zone (e.g., Lockner et al., 2000). The footwall inner damage zone in turn can accommodate less differential stress comparing to the footwall outer damage zone, leading to a higher R in the footwall inner damage zone (0.9) compared to the footwall outer damage zone (0.4). Further, the mechanically stronger hanging wall damage zone accommodate a larger differential stress, leading to a much smaller R of 0.1. Consequently, among the damage zones, the hanging wall damage zone has the largest

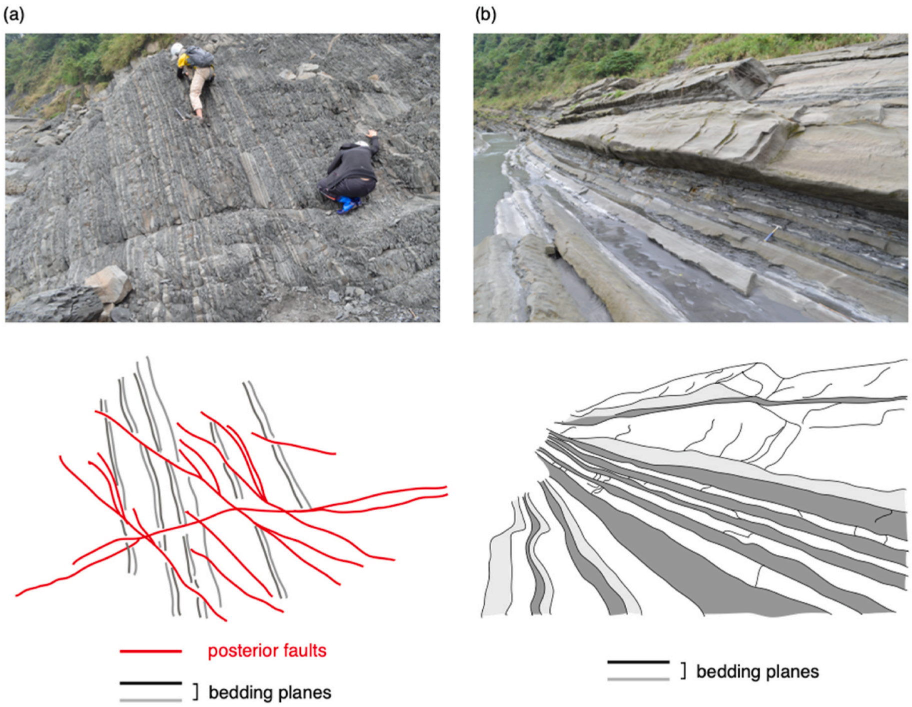

Fig. 9. Mesoscale structures in the footwall (a) outer damage zone and (c) protolith regions.

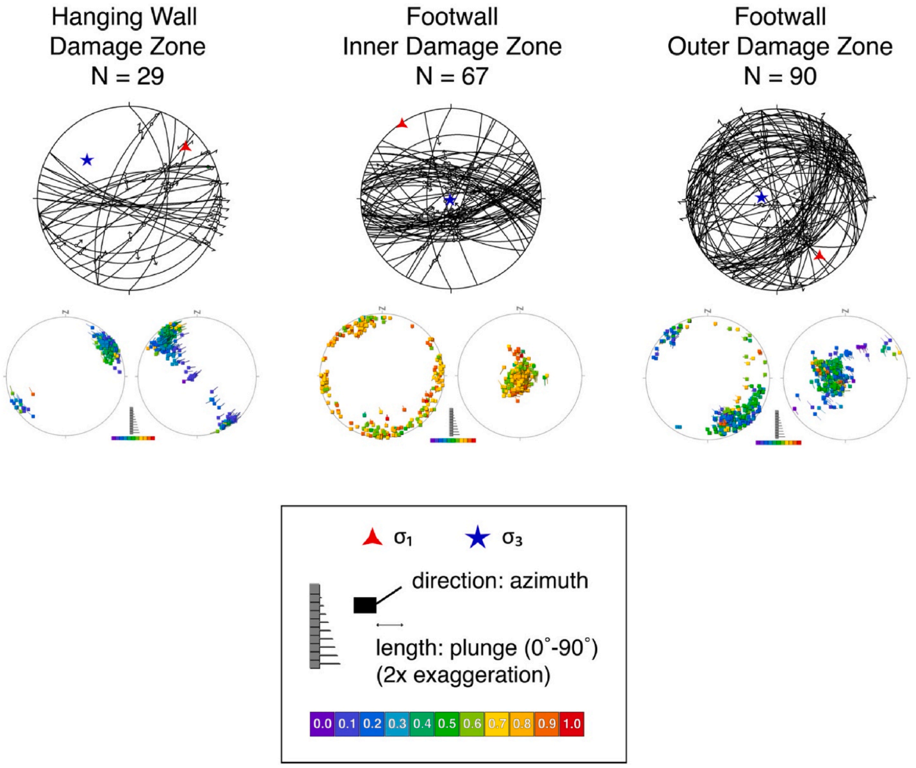

Fig. 10. Results of paleostress analysis. All calculated reduced stress tensors (i.e., one for each subset in our case) are plotted in a pair of lower-hemisphere plots: the left part of the obtained MIM plot shows the calculated directions of axes of σ_1 and the right part displays the directions of the axes of σ_3. The symbols for stress axes are color-coded according to the respective values of R $((\sigma_2 - \sigma_3)/(\sigma_1 - \sigma_3))$ that range from 0 to 1. (For interpretation of the references to color in this figure legend, the reader is referred to the Web version of this article.)

coefficient of friction, followed by the footwall outer damage zone, and then the footwall inner damage zone. Future investigations on mechanical and frictional properties of the fault rock are required to verify our interpretation.

5.3. *Ductile mode structures*

In the footwall inner damage zone, small-scale faults postdate ductile structures, which reveals a transition in deformation modes. Within the

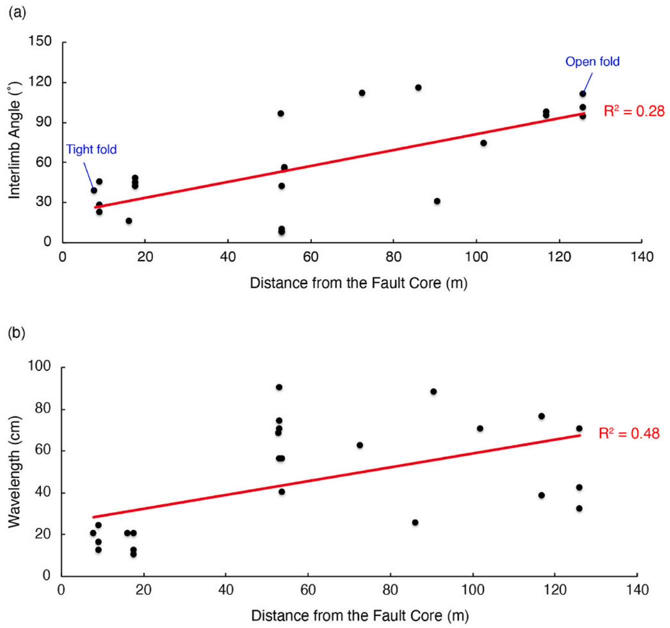

Fig. 11. (a) Interlimb angle and (b) wavelength of the folds in the footwall inner damage zone. The red lines in (a) and (b) indicate the linear best-fit of the datasets. The blue boxes refer to the field photos in Fig. 6(c). (For interpretation of the references to color in this figure legend, the reader is referred to the Web version of this article.)

ductile folds, mud-filled veins are not associated with mineral recrystallization (Fig. 7b). Such ductile structures, including folds, boudins, and mud-filled veins, are typical products of progressive soft-sediment deformation in poorly lithified sedimentary sequence due to expulsion of pore-fluid pressure, resulting in a substantial decrease in porosity (e.g., Moore and Byrne, 1987; Maltman, 1998; Nicol and Childs, 2018; Palladino et al., 2018).

The fold axes in the footwall inner damage zone are consistent with the pole of the fault core of the Chimei Fault (Fig. 12), which indicates that the development of the folds in the footwall inner damage zone may be related to the movement of the Chimei Fault activities. The deviation of the fold axes from the π plane also indicates that the folds also involve asymmetric simple shear in addition to pure shear. Such asymmetric simple shear is also shown in our field observation (Fig. 6). In addition, the poles to the fold axial planes are concentrated near the NW-SE poles of the lower-hemisphere projection, and the inferred compressional axes are consistent with the orientation of σ_1 in the footwall inner damage zone based on our paleostress analysis (Figs. 10 and 12).

Furthermore, the degree of deformation, as indicated by fold interlimb angles and wavelengths, significantly increases toward the principal slip zone of the Chimei Fault (Fig. 11). We thus interpret that the ductile structures in the footwall inner damage zone are related to the progressive deformation of the Chimei Fault and represent an initial deformation that accommodates fault activities in the footwall.

5.4. *Implications for the deformation evolution of the Chimei Fault*

The development of the gypsum veins in the hanging wall protolith has been interpreted as syn-volcanic fractures that can be dated back to Miocene (Wang and Yang, 1974; Yang et al., 1988; Song and Lo, 2002; Chen, 2005; Teng et al., 2016). Together with our observation that the gypsum veins are cut by the branch faults (Fig. 4a), we thus consider the gypsum veins to be the oldest mesoscale structure in our study area. The footwall turbidite exhibits more complicated deformation modes than the hanging wall andesite. The presence of boudins, pinch-and-swell structures, and mud-filled veins implies that the footwall sedimentary rocks were not fully lithified and remained mechanically weak during the early activities of the Chimei Fault, thus deformation was primarily accommodated by ductile structures. Such deformation behavior has been well documented in the offshore drilling sites at active subduction zones (e.g., Moore and Byrne, 1987; Maltman, 1998; Chester et al., 2013; Savage et al., 2021). These ductile features were later crosscut by brittle structures (e.g., faults, foliations), suggesting that the subsequent mode of deformation transitioned to be brittle failure in the footwall as turbidites were further lithified.

With an integration of our field-based constraints and evolution based on tectonic stratigraphy (Lai et al., 2021a, 2022), we propose a four-stage scenario to explain the transition in deformation modes (Fig. 14). (1) Miocene rock damages developed in response to syn-volcanic activities of the ancient Chimei Volcano of the Luzon Arc (Lai et al., 2017), as shown by the gypsum-filled slickenfiber in the hanging wall. (2) During ~4 to 0.8 Ma, the Taiwan arc-continent collision has influenced the study area, developing a collisional basin (retro-foredeep) on top of the forearc crust. The orogen-derived turbidites and conglomerates deposited in this collisional basin, eastward-onlapping onto of the arc basement rock. (3) Chimei Fault accommodated tectonic strain as a part of the structural inversion of the Coastal Range approximately between 0.8 and 0.5 Ma. Asymmetric folding may have been developed in response to the initiation of the Chimei fault, tilting the hanging wall rocks as well as forming a fault-parallel syncline in the footwall. During this early development stage of the Chimei Fault, the marine turbidites remained poorly consolidated nor lithified. Thus the strain was primarily accommodated by subsurface ductile deformation in the footwall. The deformation in the hanging wall may only occur within a narrow range approximal to the fault plane. (4) Since 0.8–0.5 Ma, the Chimei Fault facilitated disaggregation in the hanging wall, and the footwall turbidites became fully lithified and were able to accommodate brittle mode failure. A subsidiary spay fault developed in the SE limb of the fault-parallel

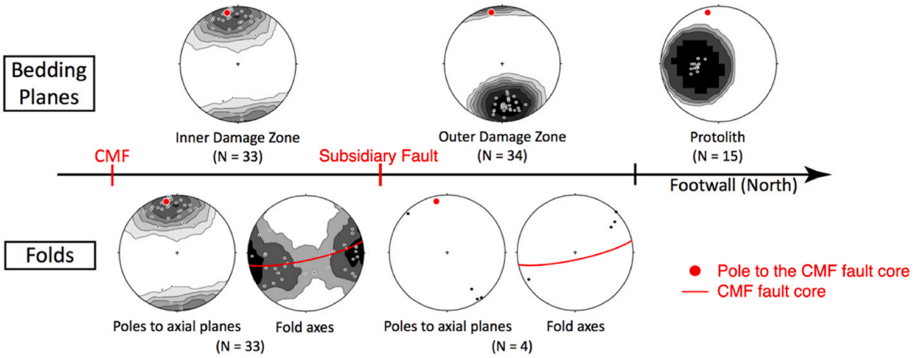

Fig. 12. Results of fold kinematic analysis. The contours indicate confidence interval of 2 standard deviations. The lower-hemisphere projections are plotted using the Stereonet software developed by Cardozo and Allmendinger (2013).

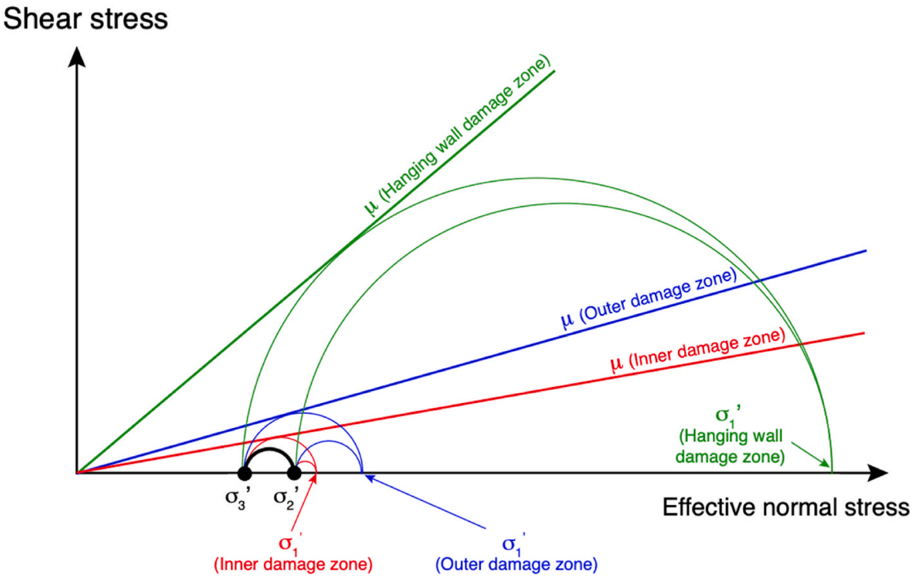

Fig. 13. Mechanical interpretations of the overprinting brittle faults in the hanging wall and brittle damage zones. σ_2' and σ_3' are assumed to be constant (color-coded in black). Mohr circles and the linear friction envelopes color-coded in red, blue, and green indicate the interpretations of the footall inner damage zone, footwall outer damage zone, and hanging wall damage zone, respectively. The relative magnitudes of the Mohr circles are plotted based on the *R* values of the footwall inner damage zone (0.9), footwall outer damage zone (0.4), and the hanging wall damage zone (0.1) (Fig. 9). (For interpretation of the references to color in this figure legend, the reader is referred to the Web version of this article.)

asymmetric syncline. This subsidiary fault further tilted the footwall inner damage zone strata and cause overprinting brittle foliations. Later in this stage, the Chimei Fault plane was steepened, and the Chimei Fault rocks in turn hosted permutation between strike-slip and reverse movement (Chen et al., 2021).

The steepening of the Chimei Fault dip may be a consequence of fault imbrication of the *en échelon* fault system in the Coastal Range in eastern Taiwan, this been implicitly proposed in some previous studies (e.g., Barrier and Angelier, 1986). The latter developed in-sequence reverse fault and associated folds (e.g., the Longitudinal Valley Fault and the Chimei Syncline) tilted and steepened the antecedent reverse fault and folds (e.g., the Chimei Fault and the fault parallel syncline) due to westward propagation of faulting (Shyu et al., 2006). As the fault core of the Chimei Fault became steeper, it began to host both strike-slip and reverse faulting movements because the dip angle of the main fault core became highly misoriented from the optimal angle for reverse faulting activity (Sibson, 1985). This is supported by recent seismicity and leveling measurements (Hsu et al., 2009; Chen et al., 2021).

We also considered the possibility that fracturing and faulting in the hanging wall in stages 3 and 4 predate shear localization along the Chimei Fault. If this scenario holds, the development of the fault core may be similar as that of the Punchbowl Fault, where comminution reworked the deformed wall rock and facilitated layering of less cohesive material (Chester and Chester, 1998).

It is worth noting that the footwall may have experienced asymmetric uplift and the posterior exhumation induced by the activities of the Chimei Fault and its subsidiary fault (Fig. 14), which leads to the contrast in deformation mechanisms across the footwall inner and outer damage zones. The sequence that has not yet exhumed beneath the footwall outer damage zone thus may also exhibit ductile mode structures related to early-stage soft sediment deformation.

5.5. *Implications for evolving mechanical characteristics within the Coastal Range*

Across the Chimei Fault core, the hanging wall damage zone exhibits an averaged σ_1-axes that is nearly perpendicular to the averaged σ_1-axes in the footwall damage zones (Fig. 10). The discrepancy in the orientation of the σ_1-axes across the main fault core may be controlled by the mechanical properties of the host rocks. As documented in Faulkner et al. (2006), elastic moduli alter the orientation of σ_1 as fault rock approaches the fault core. The relative rock strength obtained from Schmidt rebound hammer tests also reveals that the strength of the crystalline andesite (>30 MPa) is larger than that of the turbidites (<20 MPa) in the Coastal Range (Lai et al., 2021b), supporting differences in mechanical properties across the Chimei Fault.

During stage 4, a subsidiary fault developed at the frontal position from the main fault core (Fig. 14), resulting in the brittle failure propagating into the hanging wall if the differential stress exceeds the rock strength therein (Fig. 13), and, in turn, generate fault damage in response to the fault activity. Magnitude of strain across the Chimei Fault and the subsidiary fault in the footwall can be inferred from the results of the anisotropy of magnetic susceptibility (AMS) (Chu et al., 2015). Strain intensity (Int) and degree of anisotropy (P) gradually increase from the footwall inner damage zone to the fault core, as well as from the footwall outer damage zone to the subsidiary fault. Both Int and P abruptly decreases from the fault core to the hanging wall, also from the subsidiary fault to the footwall inner damage zone. The AMS results reveal that strain intensity induced by the Chimei Fault and the subsidiary fault is asymmetric across different fault zone components.

There have been similar deformation structures as the Chimei Fault rocks discovered in other regions of the Coastal Range (e.g., Teng et al., 2002; Lai and Teng, 2016). The reported mechanical characteristics of the Chimei Fault may exhibit as an exceptional example the asymmetric deformation recorded in the Plio-Pleistocene turbidites in eastern Taiwan (Lai et al., 2021a). Detailed studies on rock physics, such as hydromechanical properties and frictional behaviors, are required to more completely characterize mechanical evolution in response to rapid convergence in eastern Taiwan suture zone.

6. Conclusions

We present field observation, paleostress analysis, and fold kinematic analysis of the Chimei Fault, which juxtaposes contrasting lithological units with an andesitic complex thrusting over a turbidites. Fault damage zone is asymmetric with respect to the fault core, where the

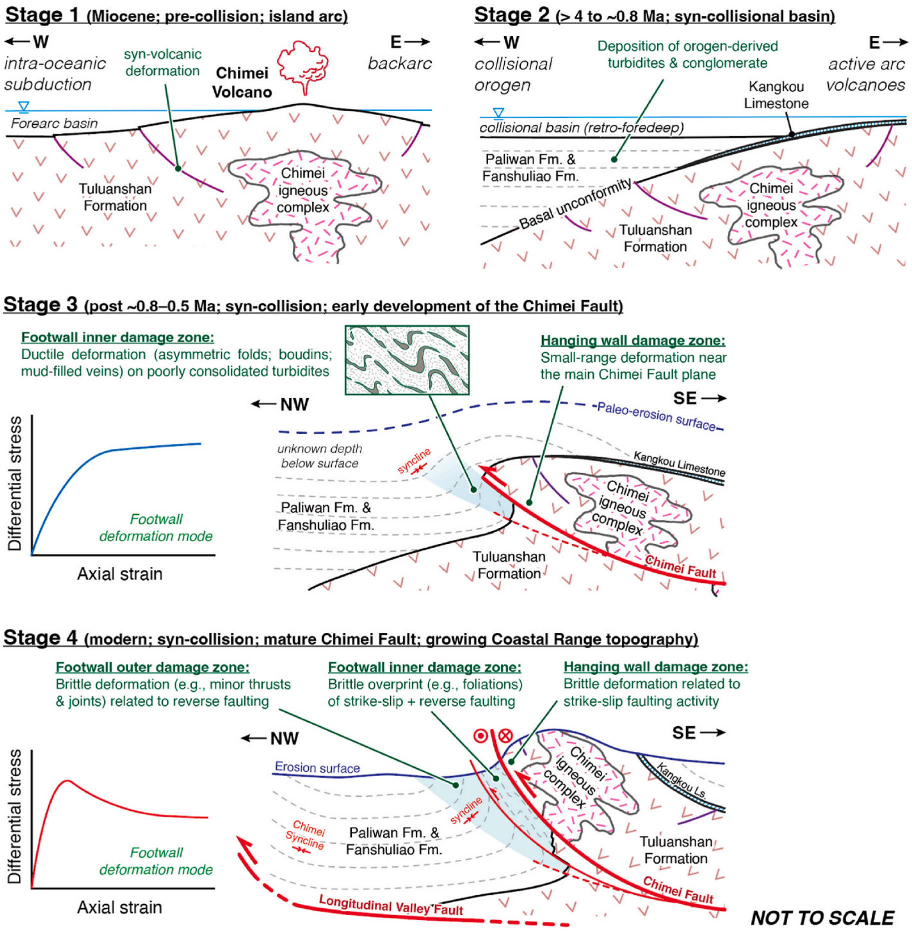

Fig. 14. Proposed four-stage structural deformation history for the Chimei region. Each stage corresponds to a major geologic event recorded in the Coastal Range stratigraphy (Lai et al., 2021a, 2022) and west-ward propagating thrust sequence. The blue shallows highlight the footwall damage zone. The left panels in stages 3 and 4 show interpretive curves of differential stress-axial strain to explain field-observed mechanical properties in the footwall damage zone in response to fault activities. See detailed discussions in Sections 5.4 and 5.5. (For interpretation of the references to color in this figure legend, the reader is referred to the Web version of this article.)

damage zone width with fracture density approaching 60 N/m in the footwall (125 m) is larger than in the hanging wall (3 m). Structural characteristics of the hanging wall damage zone and the footwall outer damage zone are dominated by brittle subsidiary faults, while those of the footwall inner damage zone show their complexity with ductile folds overprinted by the brittle subsidiary faults in the footwall inner damage zone. Our paleostress analysis shows that the hanging wall damage zone indicate NE-SW compression with stress ratio of 0.1. In contrast, σ_1 trends N40°W in the footwall damage zones with stress ratios of 0.4 and 0.9 in the footwall outer and inner damage zones, respectively. We interpret the orientation and magnitude of σ_1, as well as the stress ratio, depend on the lithology of the fault rocks, where the mechanically stronger andesite can accommodate larger differential stresses than the weaker turbidites. The orientation of the fold axial planes, together with the interlimb angles and wavelengths of the folds, show that the ductile structures in the footwall inner damage zone are the consequence of progressive soft-sediment deformation and are fault-related. Based on our field observations, we propose a four-stage evolution history to explain the predating ductile folds and the overprinting brittle faults in the Chimei area: (1) rock damages developed in response to Miocene syn-volcanic activities; (2) the orogen-derived turbidites and conglomerates deposited in a retro-foredeep basin developed above of the Luzon forearc crust; (3) Chimei Fault accommodated tectonic strain, facilitating the development of localized disaggregation in the hanging wall andesite, together with progressive and ductile deformation in the poorly lithified footwall turbidites; (4) as Chimei Fault activities progressed, the footwall turbidites became fully lithified and was able to accommodate brittle mode failure; during this stage, a new subsidiary fault formed associated with new fractures in the footwall, and the fault also hosted strike-slip faulting movement as the Chimei Fault steepened by proceeding in-sequence thrusting.

CRediT authorship contribution statement

Szu-Ting Kuo: Writing – review & editing, Writing – original draft, Visualization, Project administration, Methodology, Investigation, Formal analysis, Data curation, Conceptualization. **Larry Syu-Heng Lai:** Writing – review & editing. **En-Chao Yeh:** Resources, Investigation. **Yi-Ling Tsai:** Investigation, Data curation. **Li-Wei Kuo:** Writing – review & editing, Supervision, Funding acquisition.

Declaration of competing interest

The authors declare that they have no known competing financial interests or personal relationships that could have appeared to influence the work reported in this paper.

Data availability

Data will be made available on request.

Acknowledgement

This manuscript was greatly improved by detailed and constructive reviews from the editor, Dr. Zhikun Ren, Dr. Fabrizio Storti, and two anonymous reviewers. The authors greatly appreciate feedback and field assistance from Dr. Louis S. Teng during preliminary stages of this research. The authors thank Dr. Hiroko Kitajima for insights on an early draft of this manuscript. The authors also thank Dr. Hiroki Sone for generous feedback during revision. This research was supported by Taiwan ROC (Republic of China) National Science and Technology Council grant NSTC 112-2628-M-008-003-MY3 and NSTC 112-2119-M-213-001 to Li-Wei Kuo.

Appendix A. Supplementary data

Supplementary data to this article can be found online at https://doi.org/10.1016/j.jsg.2024.105218.

References

Aben, F.M., Doan, M.-L., Gratier, J.-P., Renard, F., 2017. High strain rate deformation of porous sandstone and the asymmetry of earthquake damage in shallow fault zones. Earth Planet Sci. Lett. 463, 81–91. https://doi.org/10.1016/j.epsl.2017.01.016.

Bai, T., Pollard, D.D., 2000. Fracture spacing in layered rocks: a new explanation based on the stress transition. J. Struct. Geol. 22 (1), 43–57. https://doi.org/10.1016/S0191-8141(99)00137-6.

Barrier, E., Angelier, J., 1986. Active collision in eastern Taiwan: The Coastal Range. Tectonophysics 125 (1–3), 39–72. https://doi.org/10.1016/0040-1951(86)90006-5.

Belzer, B.D., French, M.E., 2022. Frictional constitutive behavior of chlorite at low shearing rates and hydrothermal conditions. Tectonophysics 837, 229435. https://doi.org/10.1016/j.tecto.2022.229435.

Berg, S.S., Skar, T., 2005. Controls on damage zone asymmetry of a normal fault zone: outcrop analyses of a segment of the Moab fault, SE Utah. J. Struct. Geol. 27, 1803–1822. https://doi.org/10.1016/j.jsg.2005.04.012.

Bott, M.H.P., 1959. The mechanics of oblique slip faulting. Geol. Mag. 96, 109–117. https://doi.org/10.1017/S0016756800059987.

Caine, J.S., Evans, J.P., Forster, C.B., 1996. Fault zone architecture and permeability structure. Geology 24, 1025. https://doi.org/10.1130/0091-7613(1996)024<1025:FZAAPS>2.3.CO;2.

Cao, D., Zeng, L., Gomez-Rivas, E., Gong, L., Liu, G., Lu, G., Bons, P.D., 2024. Correction of linear fracture density and error analysis using underground borehole data. J. Struct. Geol. 184, 105152 https://doi.org/10.1016/j.jsg.2024.105152.

Cardozo, N., Allmendinger, R.W., 2013. Spherical projections with OSXStereonet. Comput. Geosci. 51, 193–205. https://doi.org/10.1016/j.cageo.2012.07.021.

Chai, B.H.T., 1972. Structure and tectonic evolution of Taiwan. Am. J. Sci. 272, 389–422. https://doi.org/10.2475/ajs.272.5.389.

Chen, H.-Y., Lee, J.-C., Tung, H., Chen, C.-L., Lee, H.K., 2021. Variable vertical movements and their deformation behaviors at convergent plate suture: 14-year-long (2004–2018) repeated measurements of precise leveling around middle Longitudinal Valley in eastern Taiwan. J. Asian Earth Sci. 218, 104865 https://doi.org/10.1016/j.jseaes.2021.104865.

Chang, C.P., Angelier, J., Huang, C.Y., Liu, C.S., 2001. Structural evolution and significance of a mélange in a collision belt: the Lichi Mélange and the Taiwan arc–continent collision. Geol. Mag. 138 (6), 633–651. https://doi.org/10.1017/S0016756801005970.

Chen, L.S., 2005. Structural Analysis of the Chimei Fault Zone, Hsiukuluan River, Coastal Range, Eastern Taiwan. Master's thesis at National Central University, p. 117p.

Chen, T.-W., Chu, M.-F., Chen, W.-S., Chung, S.-L., Lee, H.-Y., Iizuka, Y., 2023. retro-foredeep basin evolution in Taiwan: Zircon U-Pb and Hf isotope constraints from the coastal range. G-cubed 24, e2022GC010787. https://doi.org/10.1029/2022GC010787.

Cheng, W.H., 1996. A Study on the Characteristics of Geological Structures in the Northern Coastal Range, Eastern Taiwan. Master's thesis at National Cheng Kung University, p. 156p.

Chester, F.M., Chester, J.S., 1998. Ultracataclasite structure and friction processes of the Punchbowl fault, San Andreas system, California. Tectonophysics 295, 199–221. https://doi.org/10.1016/S0040-1951(98)00121-8.

Chester, F.M., Evans, J.P., Biegel, R.L., 1993. Internal structure and weakening mechanisms of the san andreas fault. J. Geophys. Res. Solid Earth 98, 771–786. https://doi.org/10.1029/92JB01866.

Chester, F.M., Logan, J.M., 1986. Implications for mechanical properties of brittle faults from observations of the Punchbowl fault zone, California. Pure and Applied Geophysics PAGEOPH 124, 79–106. https://doi.org/10.1007/BF00875720.

Chester, F.M., Rowe, C., Ujiie, K., Kirkpatrick, J., Regalla, C., Remitti, F., Moore, J.C., Toy, V., Wolfson-Schwehr, M., Bose, S., Kameda, J., Mori, J.J., Brodsky, E.E., Eguchi, N., Toczko, S., Expedition 343 and 343T Scientists, 2013. Structure and composition of the plate-boundary slip zone for the 2011 Tohoku-Oki earthquake. Science 342, 1208–1211. https://doi.org/10.1126/science.1243719.

Chu, Y.-R., Yeh, E.-C., Kuo, S.-T., 2015. Study of Magnetic Fabrics across the Central Part of the Chimei Fault, the Coastal Range of Eastern Taiwan. AGU. Abstract MR33B-2661, poster presented at 2015 Fall meeting.

Engelder, T., 1987. Joints and shear fractures in rock. Fract. Mech. Rock 2, 27–69.

Fagereng, Å., et al., 2019. Mixed deformation styles observed on a shallow subduction thrust, Hikurangi margin, New Zealand. Geology 47, 872–876. https://doi.org/10.1130/G46367.1.

Faulkner, D.R., Jackson, C.A.L., Lunn, R.J., Schlische, R.W., Shipton, Z.K., Wibberley, C.A.J., Withjack, M.O., 2010. A review of recent developments concerning the structure, mechanics and fluid flow properties of fault zones. J. Struct. Geol. 32, 1557–1575. https://doi.org/10.1016/j.jsg.2010.06.009.

Faulkner, D.R., Mitchell, T.M., Healy, D., Heap, M.J., 2006. Slip on 'weak' faults by the rotation of regional stress in the fracture damage zone. Nature 444 (7121), 922–925. https://doi.org/10.1038/nature05353.

Gross, M.R., 1993. The origin and spacing of cross joints: examples from the Monterey Formation, Santa Barbara Coastline, California. J. Struct. Geol. 15 (6), 737–751. https://doi.org/10.1016/0191-8141(93)90059-J.

Hsieh, Y.-H., Liu, C.-S., Suppe, J., Byrne, T.B., Lallemand, S., 2020. The Chimei submarine canyon and fan: a record of Taiwan arc-continent collision on the rapidly deforming over-riding plate. Tectonics 39, e2020TC006148. https://doi.org/10.1029/2020tc006148.

Hsu, T.L., 1956. Geology of the costal range, eastern Taiwan. Bull. Geol. Surv. Taiwan 8, 39–63.

Hsu, Y.-J., Yu, S.-B., Simons, M., Kuo, L.-C., Chen, H.-Y., 2009. Interseismic crustal deformation in the Taiwan plate boundary zone revealed by GPS observations, seismicity, and earthquake focal mechanisms. Tectonophysics 479, 4–18. https://doi.org/10.1016/j.tecto.2008.11.016.

Kim, Y.-S., Peacock, D.C.P., Sanderson, D.J., 2004. Fault damage zones. J. Struct. Geol. 26, 503–517. https://doi.org/10.1016/j.jsg.2003.08.002.

Kohlstedt, D.L., Evans, B., Mackwell, S.J., 1995. Strength of the lithosphere: constraints imposed by laboratory experiments. J. Geophys. Res. Solid Earth 100 (B9), 17587–17602. https://doi.org/10.1029/95JB01460.

Lai, L.S.H., Dorsey, R.J., Horng, C.S., Chi, W.R., Shea, K.S., Yen, J.Y., 2021a. Polygenetic mélange in the retrowedge foredeep of an active arc-continent collision, Coastal Range of eastern Taiwan. Sediment. Geol. 418, 105901 https://doi.org/10.1016/j.sedgeo.2021.105901.

Lai, L.S.H., Dorsey, R.J., Horng, C.S., Chi, W.R., Shea, K.S., Yen, J.Y., 2022. Extremely rapid up-and-down motions of island arc crust during arc-continent collision. Commun. Earth Environ. 3 (1), 100. https://doi.org/10.1038/s43247-022-00429-2.

Lai, L.S.-H., Roering, J.J., Finnegan, N.J., Dorsey, R.J., Yen, J.-Y., 2021b. Coarse sediment supply sets the slope of bedrock channels in rapidly uplifting terrain: field and topographic evidence from eastern Taiwan. Earth Surf. Process. Landforms 46 (13), 2671–2689. https://doi.org/10.1002/esp.5200.

Lai, L.S.-H., Teng, L.S., 2016. Stratigraphy and structure of the Tai-Yuan basin, southern coastal range, eastern Taiwan. Bull. Centr. Geol. Survey, Minist. Econ. Affairs Taiwan 45–76.

Lai, Y.-M., Song, S.-R., Lo, C.-H., Lin, T.-H., Chu, M.-F., Chung, S.-L., 2017. Age, geochemical and isotopic variations in volcanic rocks from the coastal range of Taiwan: implications for magma generation in the northern Luzon Arc. Lithos 272–273, 92–115. https://doi.org/10.1016/j.lithos.2016.11.012.

Laubach, S.E., Olson, J.E., Gross, M.R., 2009. Mechanical and fracture stratigraphy. AAPG Bull. 93 (11), 1413–1426. https://doi.org/10.1306/07270909094.

Li, H., Wang, H., Xu, Z., Si, J., Pei, J., Li, T., Huang, Y., Song, S.-R., Kuo, L.-W., Sun, Z., Chevalier, M.-L., Liu, D., 2013. Characteristics of the fault-related rocks, fault zones and the principal slip zone in the Wenchuan earthquake fault scientific drilling Project hole-1 (WFSD-1). Tectonophysics 584, 23–42. https://doi.org/10.1016/j.tecto.2012.08.021.

Lai, W.C., 1995. A Study on the Characteristics of the Structures in the Middle Part of Coastal Range, Eastern Taiwan. Master's thesis at National Cheng Kung University, 107p.

Lockner, D., Naka, H., Tanaka, Hidemi, Ito, Hisao, Ikeda, R., 2000. Permeability and strength of core samples from the Nojima fault of the 1995 Kobe earthquake. In: Ito, H., Fujimoto, K., Tanaka, H., Lockner, D.A. (Eds.), Proceedings, International Workshop on the Nojima Fault Core and Borehold Data Analysis, pp. 147–152.

Lundberg, N., Dorsey, R.J., 1988. Synorogenic sedimentation and subsidence in a Plio-Pleistocene collisional basin, eastern Taiwan. In: Kleinspehn, K., Paola, C. (Eds.), New Perspectives in Basin Analysis. Frontiers in Sedimentary Geology. Springer, New York, pp. 265–280.

Lundberg, N., Moore, J.C., 1986. Macroscopic Structural Features in Deep Sea Drilling Project Cores from Forearc Regions, vol. 166. Geological Society of America Memoir, pp. 13–44.

Ma, K.-F., Tanaka, H., Song, S.-R., Wang, C.-Y., Hung, J.-H., Tsai, Y.-B., Mori, J., Song, Y.-F., Yeh, E.-C., Soh, W., Sone, H., Kuo, L.-W., Wu, H.-Y., 2006. Slip zone and energetics of a large earthquake from the Taiwan Chelungpu-Fault Drilling Project. Nature 444, 473–476. https://doi.org/10.1038/nature05253.

Maltman, A.J., 1998. Deformation structures from the toes of active accretionary prisms. J. Geol. Soc. 155, 639–650. https://doi.org/10.1144/gsjgs.155.4.0639.

McGrath, A.G., Davison, I., 1995. Damage zone geometry around fault tips. J. Struct. Geol. 17, 1011–1024. https://doi.org/10.1016/0191-8141(94)00116-H.

Mitchell, T.M., Ben-Zion, Y., Shimamoto, T., 2011. Pulverized fault rocks and damage asymmetry along the Arima-Takatsuki Tectonic Line, Japan. Earth Planet Sci. Lett. 308, 284–297. https://doi.org/10.1016/j.epsl.2011.04.023.

Moore, J.C., Byrne, T., 1987. Thickening of fault zones: a mechanism of melange formation in accreting sediments. Geology 15, 1040–1043. https://doi.org/10.1130/0091-7613(1987)15<1040:TOFZAM>2.0.CO;2.

Narr, W., Suppe, J., 1991. Joint spacing in sedimentary rocks. J. Struct. Geol. 13 (9), 1037–1048. https://doi.org/10.1016/0191-8141(91)90055-N.

Nicol, A., Childs, C., 2018. Cataclasis and silt smear on normal faults in weakly lithified turbidites. J. Struct. Geol. 117, 44–57. https://doi.org/10.1016/j.jsg.2018.06.017.

Ogata, K., Storti, F., Balsamo, F., Tinterri, R., Bedogni, E., Fetter, M., Gomes, L., Hatushika, R., 2017. Sedimentary facies control on mechanical and fracture stratigraphy in turbidite. GSA Bull. 129 (1–2), 76–92. https://doi.org/10.1130/B31517.1.

Palladino, G., Alsop, G.I., Grippa, A., Zvirtes, G., Phillip, R.P., Hurst, A., 2018. Sandstone-filled normal faults: a case study from central California. J. Struct. Geol. 110, 86–101. https://doi.org/10.1016/j.jsg.2018.02.013.

Paterson, M., Wong, T.-F., 2005. Experimental Rock Deformation — the Brittle Field. Springer-Verlag, Berlin/Heidelberg. https://doi.org/10.1007/b137431.

Pizzati, M., Balsamo, F., Storti, F., 2023. Fingerprints and energy budget of the earthquake cycle in shallow sediments. J. Struct. Geol. 170, 104858 https://doi.org/10.1016/j.jsg.2023.104858.

Rawling, G.C., Goodwin, L.B., 2006. Structural record of the mechanical evolution of mixed zones in faulted poorly lithified sediments, Rio Grande rift, New Mexico, USA. J. Struct. Geol. 28, 1623–1639. https://doi.org/10.1016/j.jsg.2006.06.008.

Savage, H.M., Shreedharan, S., Fagereng, Å., Morgan, J.K., Meneghini, F., Wang, M., McNamara, D.D., Wallace, L.M., Saffer, D.M., Barnes, P.M., Petronotis, K.E., LeVay, L.J., 2021. Asymmetric brittle deformation at the Pāpaku fault, Hikurangi subduction margin, NZ, IODP expedition 375. G-cubed 22. https://doi.org/10.1029/2021GC009662.

Shyu, J.B.H., Sieh, K., Avouac, J.-P., Chen, W.-S., Chen, Y.-G., 2006. Millennial slip rate of the Longitudinal Valley fault from river terraces: implications for convergence across the active suture of eastern Taiwan. J. Geophys. Res. 111, B08403 https://doi.org/10.1029/2005JB003971.

Sibson, R.H., 1977. Fault rocks and fault mechanisms. J. Geol. Soc. 133 (3), 191–213. https://doi.org/10.1144/gsjgs.133.3.0191.

Sibson, R.H., 1985. A note on fault reactivation. J. Struct. Geol. 7, 751–754. https://doi.org/10.1016/0191-8141(85)90150-6.

Sippel, J., Scheck-Wenderoth, M., Reicherter, K., Mazur, S., 2009. Paleostress states at the south-western margin of the Central European Basin System — application of fault-slip analysis to unravel a polyphase deformation pattern. Tectonophysics 470, 129–146. https://doi.org/10.1016/j.tecto.2008.04.010.

Smith, Z.D., Griffith, W.A., 2022. Lithological controls on fault damage zone development by coseismic tensile loading. Tectonophysics 838, 229471. https://doi.org/10.1016/j.tecto.2022.229471.

Song, S.-R., Kuo, L.-W., Yeh, E.-C., Wang, C.-Y., Hung, J.-H., Ma, K.-F., 2007. Characteristics of the lithology, fault-related rocks and fault zone structures in TCDP Hole-A. Terr. Atmos. Ocean Sci. 18, 243. https://doi.org/10.3319/TAO.2007.18.2.243(TCDP.

Song, S.-R., Lo, H.-J., 2002. Lithofacies of volcanic rocks in the central Coastal Range, eastern Taiwan: implications for island arc evolution. J. Asian Earth Sci. 21, 23–38. https://doi.org/10.1016/S1367-9120(02)00003-2.

Teng, L.S., 1990. Geotectonic evolution of late Cenozoic arc-continent collision in Taiwan. Tectonophysics 183, 57–76. https://doi.org/10.1016/0040-1951(90)90188-E.

Teng, L.S., Lee, J.-C., Heu, C.-B., 2002. Soft-sediment deformation in the fanshuliao formation of the coastal range, eastern taiwan. Bull. Cent. Geol. Surv. 15, 103–137.

Teng, L.S., Tsai, Y.L., Kuo, S.T., 2016. On the Chimei fault zone of the coastal range, eastern Taiwan. Bull. Cent. Geol. Surv. 29, 1–44.

Wallace, R.E., 1951. Geometry of shearing stress and relation to faulting. J. Geol. 59, 118–130. https://doi.org/10.1086/625831.

Wang, Y., Chen, W.-S., 1996. Hai-an range in eastern Taiwan. Geol. Ser. Taiwan 7.

Wang, Y., Yang, C.-N., 1974. Geology and copper deposits of Chimei area, coastal range, Taiwan. Natl. Sci. Counc. Proc. 1, 1–23.

Yamaji, A., 2000. The multiple inverse method: a new technique to separate stresses from heterogeneous fault-slip data. J. Struct. Geol. 22, 441–452. https://doi.org/10.1016/S0191-8141(99)00163-7.

Yang, T.-Y.F., Liu, T.-K., Chen, C.-H., 1988. Thermal event records of the Chimei igneous complex: constraint on the ages of magma activities and the structural implication based on fission track dating. Sci. Rep. Natl. Taiwan Univ. ACTA Geol. Taiwanica 26, 237–246.

Yu, S.-B., Chen, H.-Y., Kuo, L.-C., 1997. Velocity field of GPS stations in the Taiwan area. Tectonophysics 274 (1–3), 41–59. https://doi.org/10.1016/S0040-1951(96)00297-1.